Counter-gradient subgrid-scale transport and energy backscatter in turbulent deflagrations

By J. O'Brien, J. Urzay, A. Y. Poludnenko†, P. E. Hamlington‡ AND M. Ihme

Direct Numerical Simulations (DNS) of a turbulent premixed flame are performed in this study. The numerical results are differentially filtered to carry out *a priori* analyses of the interscale transfer of kinetic energy between subgrid and supergrid levels in LES. Thermal-expansion-driven backscatter of kinetic energy is found to prevail over forwardscatter throughout the entire flame brush in a manner that is interrelated with counter-gradient diffusion of scalars and with non-Boussinesq transport of momentum.

1. Introduction

The deployment of chemical energy in combustion reactions leads to thermal expansion in flames. In turbulent combustion, flame scales typically correspond to regions near the high wavenumber end of the inertial subrange or within the Kolmogorov range. The resulting decrease in density caused by combustion influences the transport of momentum, mass, and thermal energy. The extent to which thermal-expansion effects modify the inter-scale transfer of energy in turbulent combustion is largely unknown. Of particular interest for developing LES predictive capabilities of limit phenomena is the study of localized effects of combustion-driven overflow of subgrid energy in turbulent deflagrations.

In analyzing inter-scale transfer of energy in turbulent flows, it is expedient to refer to the concept of backscatter. Specifically, backscatter is understood as the transfer of kinetic energy from the smallest scales in a flow (in LES, the subgrid) back to the larger (resolved or supergrid) scales, or equivalently, the local reversal of the kinetic-energy cascade. Early works on incompressible homogeneous isotropic turbulence provided an explanation of backscatter using the spectral form of the kinetic-energy equation, while attributing backscatter to non-linear, non-local triadic interactions between relatively similar scales that exhibited a reverse-cascading tendency (Domaradzki & Rogallo 1990). Extensions that account for compressibility effects on spectral kinetic-energy transfer in homogeneous isotropic turbulence have been made previously in numerous studies (see Sagaut & Cambon (2008) for a seminal review). It should be emphasized, however, that the spectral representation of backscatter is contingent on the utilization of the Fourier basis as the dissecting mathematical tool. As a result, practically insurmountable limitations arise from using the Fourier basis to describe the energy cascade in inhomogeneous flows with variable density, variable thermodynamic coefficients, and exponentially non-linear chemical sources, as in turbulent combustion.

In a study that departed from turbulence homogeneity, Piomelli *et al.* (1991) focused on backscatter understood as the reverse flux of energy at scales comparable to the LES grid size. For that purpose, they filtered the solution of an incompressible turbulent channel-flow DNS and evaluated the SGS dissipation. Their results indicated that local

† Laboratories for Computational Physics and Fluid Dynamics, Naval Research Laboratory
‡ Department of Mechanical Engineering, University of Colorado at Boulder

backscatter of kinetic energy from the subgrid to the supergrid occurred only slightly less frequently than forwardscatter, while its intensity was of roughly the same magnitude as the forwardscatter, thus suggesting that the mean SGS dissipation was the difference between those two much larger quantities. In addition, their findings suggested that backscatter statistics were essentially independent of the choice of filtering technique, aside from some sensitivity in the intensity magnitude itself.

Employing an approach similar to Piomelli *et al.* (1991), Aluie *et al.* (2012) analyzed the effects of flow divergence on kinetic-energy transfer in the context of high-Mach number compressible homogeneous isotropic turbulence. Specifically, compressibility was identified as a mechanism that interfered with the otherwise conservative kinetic-energy cascade found in incompressible flows by enabling exchange between thermal and kinetic energies within a scale interval that spanned from large eddies down to a cutoff size, whose magnitude became increasingly smaller as the turbulent Mach number increased. In the problem studied by Aluie *et al.* (2012), however, compressibility was forced from the large scales, a situation which at first sight departs from the one typically found in combustion, namely, the concomitant generation of flow divergence at small scales (of the same order as the flame width) in low-Mach number flames.

Effects of compressibility, statistical inhomogeneity, and combustion chemical reactions on turbulence characteristics were examined in a recent study on the dynamics of the resolved kinetic energy in supersonic non-premixed turbulent flames (O'Brien *et al.* 2014). Differentially filtering DNS results showed a correlation between backscatter and flow expansion, which suggested potential combustion-driven reverse-cascade transport that could not be fully isolated from compressibility effects because of the high Mach numbers and numerous shock waves involved. However, contrary to premixed flames, the heat release in diffusion flames has a vanishing effect on the turbulent cascade, since the combustion energy is predominantly deployed within the smallest eddies where molecular mixing occurs and forward dissipation dominates (Knauss & Pantano 2009).

In this study, numerical experiments in DNS are employed to study the inter-scale transfer of energy in LES of deflagrations propagating through forced turbulence. The remainder of this report is structured as follows. In Section 2, the formulation and computational setup are briefly outlined. Section 3 is devoted to budgeting the resolved kinetic-energy equation. Section 4 studies the relation between backscatter and the depletion of SGS variances of thermal energy and mass fraction. Section 5 is focused on studying the counter-gradient transport of scalars. Finally, conclusions are drawn in Section 6.

2. Formulation and computational setup

In this study, the unsteady, compressible, reacting Navier-Stokes equations

$$\frac{\partial \rho}{\partial t} + \frac{\partial}{\partial x_i}(\rho u_i) = 0, \tag{2.1}$$

$$\frac{\partial}{\partial t}(\rho u_i) + \frac{\partial}{\partial x_j}(\rho u_i u_j) = -\frac{\partial P}{\partial x_i} + \frac{\partial \tau_{ij}}{\partial x_j}, \tag{2.2}$$

$$\frac{\partial}{\partial t}(\rho c_v T) + \frac{\partial}{\partial x_j}(\rho c_v T u_j) = -P\Delta_v + \tau_{ij}\frac{\partial u_i}{\partial x_j} + \frac{\partial}{\partial x_j}\left(\lambda \frac{\partial T}{\partial x_j}\right) + \rho q \dot{\omega}, \tag{2.3}$$

$$\frac{\partial}{\partial t}(\rho Y) + \frac{\partial}{\partial x_j}(\rho Y u_j) = \frac{\partial}{\partial x_j}\left(\rho D \frac{\partial Y}{\partial x_j}\right) - \rho \dot{\omega}, \tag{2.4}$$

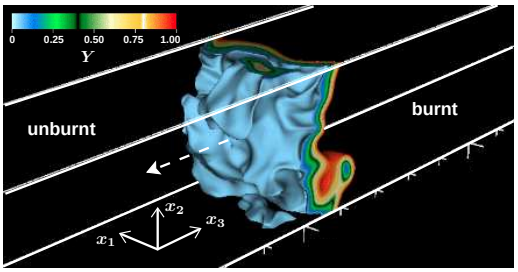

FIGURE 1. Sample snapshot from the simulations.

are integrated numerically. In the formulation, ρ is the density, u_i is the velocity, T the temperature, P the thermodynamic pressure, Y the product mass fraction, c_v the constant-volume specific heat, and λ and D the thermal conductivity and mass diffusivity, respectively. Additionally, $\tau_{ij} = 2\mu S_{ij} + (\kappa - 2\mu/3)\Delta_v \delta_{ij}$ is the viscous stress tensor, with μ being the dynamic viscosity, κ the bulk viscosity, and $S_{ij} = (1/2)(\partial u_i/\partial x_j + \partial u_j/\partial x_i)$ is the strain-rate tensor, with $\Delta_v = \partial u_i/\partial x_i$ being the flow dilatation. A constant specific heat is used in the calculations, while temperature-dependent values of viscosity, thermal conductivity, bulk viscosity, and mass diffusivity are employed according to a power law with temperature exponent 0.7. A single-step, unimolecular, irreversible Arrhenius reaction is assumed that releases q units of chemical heat per unit mass of fuel burnt, and for which the chemical source term in Eqs. (2.3) and (2.4) can be expressed as $\dot{\omega} = \rho A(1-Y)\exp(-T_a/T)$, where A and T_a are the pre-exponential factor and activation temperature, respectively. Equations (2.1)-(2.4) are supplemented with the equation of state $P = \rho R_g T$, with R_g being the gas constant. A one-dimensional asymptotic analysis of Eqs. (2.1)-(2.4) can be performed at large activation energies, in absence of free-stream turbulence, and for equidiffusive flames, to obtain the laminar flame speed $S_L = [2A\rho_u D_{T,u}(1-\alpha)\beta^{-2}\exp(-T_a/T_b)]^{1/2}$, where $\alpha = (T_b - T_u)/T_b$ is the thermal expansion coefficient, $\beta = \alpha T_a/T_b$ is the Zel'dovich number, and the subindexes $_b$ and $_u$ refer to burnt and unburnt conditions, respectively. The velocity scale S_L, along with the flame width $\delta_L \sim D_T/S_L$ (with D_T the average thermal diffusivity), are used below for estimating the characteristic dimensionless parameters of the problem.

A sample snapshot from the computations is shown in Figure 1 along with the employed coordinate system. A DNS-tailored version of the Athena-RFX reacting compressible code (Hamlington *et al.* 2011) was used in the computations that incorporates molecular-transport fluxes. The numerical scheme is explicit, with third-order spatial and second-order temporal discretization accuracies. The calculation was conducted on a structured uniform cartesian grid with $256\times256\times8192$ elements in the x_1, x_2, and x_3 directions, respectively, with x_2 and x_3 corresponding to periodic directions (e.g.m see Figure 1). The corresponding domain length in physical units was $8\delta_L \times 8\delta_L \times 256\delta_L$. This numerical resolution provided 32 cells per flame thickness δ_L, and 1.0 cells per Kolmogorov length ℓ_k in the unburnt mixture, where the viscosity is smallest and turbulence was least resolved.

Homogeneous isotropic turbulent motion was forced in the entire computational domain by injecting kinetic-energy fluctuations at wavenumbers corresponding to the spanwise length of the computational domain. Additional details about the forcing procedure are available elsewhere (Hamlington *et al.* 2011). The computations were first run without chemical source terms in a triply periodic domain to allow the turbulence to reach a statistically stationary state. Once the mixture is ignited, the domain is treated as doubly periodic in the spanwise directions x_1 and x_2, while zero-gradient boundary conditions

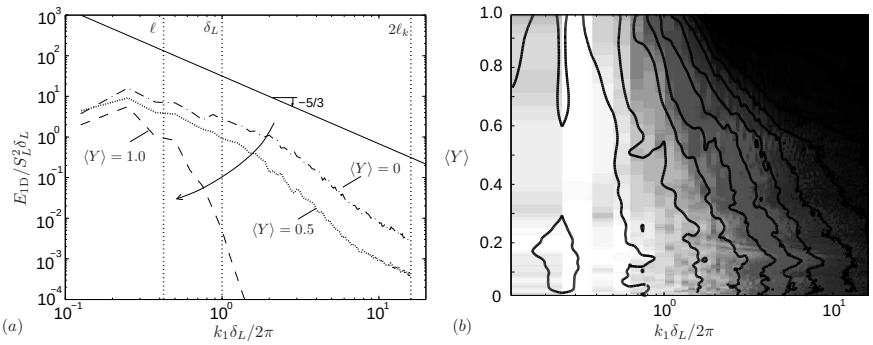

FIGURE 2. (a) Line profiles and (b) surface contours of the one-dimensional kinetic-energy spectrum along x_1 as a function of the planar-averaged product mass fraction.

are applied at the upstream and downstream boundaries. Results are analyzed after 5.6 integral times ℓ/u_ℓ have passed since ignition, during which the flame traveled a distance comparable to 4 integral length scales ℓ.

Relevant dimensionless parameters of the simulations are listed in Table 1. The computations were designed to maximize scale separation between the laminar-flame thickness δ_L and the Kolmogorov length ℓ_k in the fresh gases (within the inherent limitations of DNS-resolution cost). This allowed for deployment of combustion energy across a wide range of turbulent scales rather than constraining it to the high wavenumber range, where molecular dissipation dominates. In addition, special focus was directed to parameter regimes that enhanced counter-gradient turbulent diffusion, for which the integral velocity scale was set to be comparable to the characteristic velocity augmentation of the burnt gases through the flame due to thermal expansion. Compressibility effects were minimized by imposing small turbulence intensities and small flame speeds in comparison with the speed of sound, by which the viscous dissipation term in Eq. (2.3) became negligible along with the spatial variations of the thermodynamic pressure in Eq. (2.2). The resulting set of parameters, whose definitions can be found in the literature (Bray 1995; Peters 2000), involved order-unity Damköhler, Karlovitz and Bray numbers, while the Taylor-Reynolds number was moderately large in order to warrant separation of scales.

It should be emphasized, however, that the release of chemical energy increased the products temperature in the simulations by a factor of order $(1-\alpha)^{-1} \sim 7$, which led to a 28-fold increase in the kinematic viscosity on the burnt side of the flame. This effect, in turn, reduced the value of the Taylor-Reynolds number Re_λ listed in Table 1 down to 17.05 on the products side, which led to a 10-fold decrease in the Kolmogorov length and strongly attenuated the high-wavenumber energy of the turbulence in that region. These considerations are illustrated in the one-dimensional kinetic-energy spectra shown in Figure 2 as a function of the planar-averaged product mass fraction.

The differential-filtering procedure follows earlier work by O'Brien *et al.* (2014). In the present study, however, the width of the filter h is kept constant and equal to the laminar flame thickness δ_L. Effects of filter type on the evaluation of SGS energy dynamics are briefly discussed in Section 5. In addition, the filtering-operator notation follows the same convention as in O'Brien *et al.* (2014) for any fluid variable f, with $\overline{f}$, $\widetilde{f}$ indicating filtered and Favre-filtered values, respectively, while $\langle\overline{f}\rangle$ denotes the spanwise planar average of filtered variables.

α	0.9	thermal expansion coefficient
Le	1.0	Lewis number
Ka	2.8	Karlovitz number
Da	1.2	Damköhler number
Re_λ	95.0	Taylor-Reynolds number
N_B	2.9	Bray number
u_ℓ/S_L	2.1	turbulence intensity
Ma_L	0.01	Mach number
β	5.6	Zel'dovich number
h/δ_L	1.0	filter to laminar-flame width ratio

TABLE 1. Characteristic dimensionless parameters, with Ka, Da, Re_λ and Ma_L being evaluated on the unburnt side of the flame.

3. Kinetic-energy transfer dynamics in the turbulent flame brush

Upon multiplying the momentum equation (2.2) by $\widetilde{u}_i$, the transport equation

$$\frac{\partial \overline{\rho} k}{\partial t} + \frac{\partial}{\partial x_i}(\overline{\rho}\widetilde{u}_i k) = \alpha_\Pi + \alpha_{\mathrm{SGS}} + \alpha_v + \Pi - \epsilon_v - \epsilon_{\mathrm{SGS}} \tag{3.1}$$

is obtained for the resolved kinetic energy $k = \widetilde{u}_i\widetilde{u}_i/2$. In this formulation, α_Π, α_v, and α_{SGS} are given by

$$\alpha_\Pi = -\frac{\partial}{\partial x_i}\left(\overline{p'}\widetilde{u}_i\right), \quad \alpha_v = \frac{\partial}{\partial x_j}\left(\overline{\tau}_{ij}\widetilde{u}_i\right), \quad \alpha_{\mathrm{SGS}} = -\frac{\partial}{\partial x_j}\left(\mathcal{T}_{ij}\widetilde{u}_i\right), \tag{3.2}$$

which represent the surface work done by the pressure, viscous, and SGS turbulent forces, respectively. In Eq. (3.2), $\mathcal{T}_{ij} = \overline{\rho}(\widetilde{u_i u_j} - \widetilde{u}_i\widetilde{u}_j)$ is the SGS stress tensor, and $\overline{p'} = \overline{P} - P_0$ is the filtered hydrodynamic pressure (a quantity of order $\mathrm{Ma}_L^2 P_0 \ll P_0$), with P_0 the pressure level at an arbitrary point in the flow field. While α_Π and α_v are closed terms, the surface work done by the subgrid α_{SGS} depends on the unclosed SGS stress tensor and therefore carries information of the subgrid dynamics.

The remaining terms Π, ϵ_{SGS} and ϵ_v on the right-hand side in Eq. (3.1) are defined as

$$\Pi = \overline{p'}\widetilde{\Delta}_v, \quad \epsilon_v = \overline{\tau}_{ij}\widetilde{S}_{ij}, \quad \epsilon_{\mathrm{SGS}} = -\mathcal{T}_{ij}\widetilde{S}_{ij}, \tag{3.3}$$

where $\widetilde{\Delta}_v$ and $\widetilde{S}_{ij}$ are, respectively, the divergence and strain rate of the resolved velocity field. In particular, Π and ϵ_v are closed terms that represent, respectively, the internal-energy variations due to the work of resolved flow expansion against the hydrodynamic pressure, and the dissipation of kinetic energy caused by the filtered molecular transport. Of particular interest is the unclosed SGS dissipation ϵ_{SGS}, which is not a true dissipation as it involves only inertial dynamics, and is the prevailing mechanism of kinetic-energy transfer between the subgrid and supergrid at high Reynolds numbers. Specifically, $\epsilon_{\mathrm{SGS}} < 0$ corresponds to backscatter of kinetic energy from the subgrid (O'Brien *et al.* 2014).

The mechanism by which anisotropy is developed in the velocity field through the flame has been studied in earlier works (Aldredge & Williams 1991; Hamlington *et al.* 2011). A similar effect occurs in the resolved and subgrid velocity fields. To illustrate this, the component-wise variations of the planar-averaged resolved and SGS kinetic energies, k and k_{SGS}, with $k_{\mathrm{SGS}} = (\widetilde{u_i u_i} - \widetilde{u}_i\widetilde{u}_i)/2$, are shown in Figure 3(a,b). In particular, while the spanwise components undergo relatively slow variations, the streamwise resolved kinetic energy is enhanced through the flame in both resolved and subgrid scales. However, the corresponding enhancement of streamwise k_{SGS} is short-lived, in that the increase of viscosity on the products side rapidly attenuates this updraft of SGS energy.

The volume integrals of α_Π, α_v, and α_{SGS} vanish in triply periodic problems such

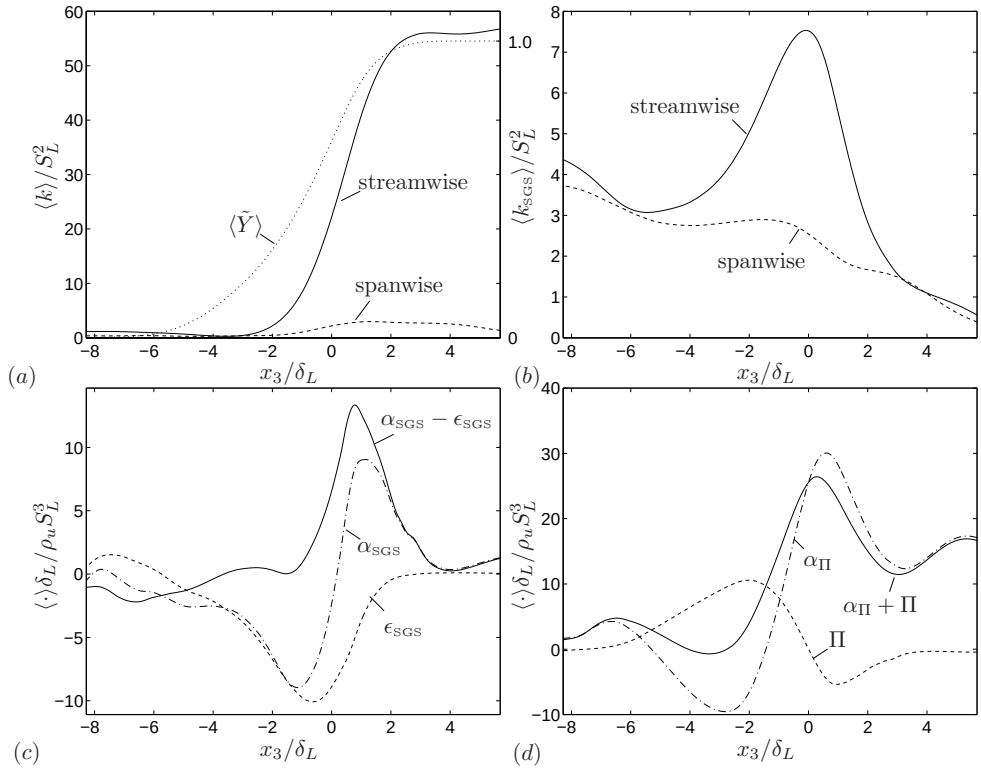

FIGURE 3. Planar-averaged distributions of (a) resolved and (b) subgrid kinetic energies, including streamwise and averaged spanwise components, along with (c) SGS momentum and (d) pressure-work transport terms in Eq. (3.1). The planar average of the filtered product mass fraction, centered at the streamwise location of maximum slope, is included in panel (a) for illustration of reaction progress.

as homogeneous isotropic turbulence, and in particular types of inhomogeneous flows such as temporal mixing layers or periodic turbulent channels. In those scenarios, the volumetric statistics of the resolved kinetic energy are modulated by the remaining terms Π, $\epsilon_{\rm SGS}$, and, to a lesser extent, ϵ_v (Aluie *et al.* 2012; O'Brien *et al.* 2014). On the other hand, in general inhomogeneous flows, all four terms on the right-hand side of Eq. (3.1) in principle participate in the conversion of kinetic energy. For instance, in the turbulent deflagration analyzed here, spanwise integration of α_Π, α_v, and $\alpha_{\rm SGS}$ leads to a one-dimensional transport equation of the planar-averaged flux of resolved kinetic energy along x_3,

$$\langle \overline{\rho}\widetilde{u}_3 k \rangle \sim -\langle \overline{\overline{p}'}\widetilde{u}_3 \rangle - \langle \mathcal{T}_{3,3}\widetilde{u}_3 \rangle - \int_{-\infty}^{x_3} \langle \epsilon_{\rm SGS} \rangle dx_3 + \int_{-\infty}^{x_3} \langle \Pi \rangle dx_3 + c_1, \tag{3.4}$$

where c_1 is a constant of integration that depends on upstream turbulence conditions. While the first two terms on the right-hand side of Eq. (3.4) distribute kinetic energy through the flame in the streamwise direction, the third and fourth terms inject or destroy energy as a result of spanwise collective effects, as shown in Figure 3(c,d), thereby making $\epsilon_{\rm SGS}$ a quantity that in principle is not fully conserved through the spanwise turbulent cascade. By way of contrast, in incompressible forced homogeneous isotropic turbulence, the cumulative effects of the first and second terms vanish due to the periodicity of

events and so does the fourth term because of flow solenoidality, while a net effect of the SGS dissipation, in principle independent of the filter width, remains after full-volume integration that balances the large-scale forced injection of energy and suffices to describe the statistical dynamics of the turbulent kinetic energy.

Combustion in the flame leads to an increase of resolved thermal energy and subsequent large-scale flow dilatation. At low Mach numbers, only a small amount of this thermal energy excess (proportional to $\mathrm{Ma}_L^2 \ll 1$) is transformed into kinetic energy through the resolved pressure-dilatation work Π in Eq. (3.1). The corresponding amount of kinetic energy generated this way is, however, sufficient to compete with the backscatter of kinetic energy from the subgrid, as shown in Figure 3(c,d) and described below.

It is worth highlighting the planar-averaged backscatter of SGS kinetic energy that occurs persistently in Figure 3(c) throughout the entire flame brush. Despite the prevailing importance of the combination $\alpha_{\mathrm{SGS}} - \epsilon_{\mathrm{SGS}}$ for generating kinetic energy in this inhomogeneous flow, emphasis is purposely placed here on the spatially coherent distribution of backscatter $\epsilon_{\mathrm{SGS}} < 0$ in the flame, since Boussinesq models of turbulent transport typically feed directly on strictly dissipative models of the former. To see this, consider the standard Boussinesq closure model

$$\mathcal{T}_{ij} - \frac{2}{3}\overline{\rho}k_{\mathrm{SGS}}\delta_{ij} = -2\overline{\rho}\nu_t\left(\widetilde{S}_{ij} - \frac{\widetilde{\Delta}_v\delta_{ij}}{3}\right) \tag{3.5}$$

for the SGS turbulent stress tensor. In Eq. (3.5), ν_t represents an unknown scalar eddy viscosity, whose magnitude depends on the filter width. In principle, Eq. (3.5) represents an overdetermined system of five independent equations. In the present calculations, however, the largest contribution to ν_t is produced by the positive normal strain rate $\widetilde{S}_{3,3}$ because of the dominant thermal expansion effect along the same direction (and given also the fact that the flame is not excessively contorted). This suggests a tendency towards reverse (-x_3 direction) unresolved turbulent transport when $\mathcal{T}_{3,3}$ is computed by evaluating the right-hand side of Eq. (3.5) using, for instance, a strictly dissipative representation of ν_t such as the Smagorinsky model. Results from the filtered DNS indicate, on the other hand, that $\mathcal{T}_{3,3}$ is larger than the hydrostatic (isotropizing) SGS stress $-2\overline{\rho}k_{\mathrm{SGS}}/3$, and therefore the unresolved turbulent transport has an anomalous (or non-Boussinesq) tendency to occur in the forward ($+x_3$) streamwise direction. The discrepancy can be understood by noticing that $\mathcal{T}_{3,3}/\overline{\rho}$ equals twice the SGS kinetic energy in the streamwise direction, which undergoes an unparalleled sharp increase in the flame, as shown in Figure 3(b). Because of this anisotropy induced by the thermal expansion, the resulting streamwise SGS kinetic energy is much larger than the corresponding average value per spatial direction, $k_{\mathrm{SGS}}/3$, the energy excess being proportional to the tendency towards non-Boussinesq transport. Nonetheless, it could be expected that Eq. (3.5) may still render a globally positive ν_t and subsequent Boussinesq-like transport as a result of counteracting three-dimensional effects. That this is not the case in the strongly anisotropic flow encountered in the present study can be understood by formally relating the anomalous transport of momentum to SGS backscatter, for which we contract Eq. (3.5) with $\widetilde{S}_{ij}$ as in the original dynamic Smagorinsky procedure to obtain the expression

$$\nu_t = \frac{\epsilon_{\mathrm{SGS}} + (2/3)\widetilde{\rho}k_{\mathrm{SGS}}\widetilde{\Delta}_v}{2\overline{\rho}\left(|\widetilde{S}|^2 - \widetilde{\Delta}_v^2/3\right)} \tag{3.6}$$

that accounts for the three directions. Note that Lilly's least-squares approach provides

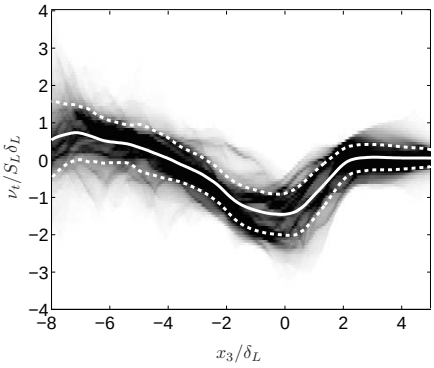

FIGURE 4. Contours of the PDF of eddy viscosity ν_t conditioned on the streamwise coordinate x_3, along with mean (solid line) and standard deviation (dashed lines).

qualitatively similar results for the purposes of this discussion. The denominator in Eq. (3.6) is a positive quadratic form. Conversely, in the numerator of Eq. (3.6), the persistent SGS backscatter in the flame drives ν_t towards negative values, while the second term, which involves the work done by the subgrid dynamic pressure against the flow dilatation, tends to restore ν_t to positive values by isotropizing the transport, both terms being comparable in the simulations. The net outcome, however, is a predominantly negative eddy viscosity throughout the flame, as shown in Figure 4, with exceptions upstream where homogeneous isotropic dynamics are dominant, thereby suggesting that the strong anisotropic effect caused by thermal expansion supersedes any transversal restoration and renders global non-Boussinesq transport in the three spatial directions.

4. Joint statistics between kinetic-energy backscatter and depletion of SGS variances of thermal energy and mass fraction

Subtraction of Eq. (3.1) from the transport equation of the filtered kinetic energy, $\widetilde{K} = \widetilde{u_i u_i}/2$, leads to the transport equation for $k_{\rm SGS}$

$$\frac{\partial}{\partial t}(\overline{\rho}k_{\rm SGS}) + \frac{\partial}{\partial x_i}(\overline{\rho}\widetilde{u}_i k_{\rm SGS}) = \frac{\partial}{\partial x_i}\left(\overline{p'\widetilde{u}_i} - \overline{p'u_i} + \overline{\tau_{ij}u_j} - \overline{\tau}_{ij}\widetilde{u}_j + \mathcal{T}_{ij}\widetilde{u}_i + \overline{\rho}\widetilde{u}_i\widetilde{K} - \overline{\rho}\widetilde{u_i K}\right) + \overline{p'\Delta_v} - \overline{p'}\widetilde{\Delta}_v + \overline{\tau}_{ij}\widetilde{S}_{ij} - \overline{\tau_{ij}S_{ij}} + \epsilon_{\rm SGS}. \tag{4.1}$$

In particular, dynamic models of eddy viscosity often rely on Eq. (4.1) as an additional constraint in energy repartition (Ghosal *et al.* 1995), which here should account for the competition between backscatter and thermal expansion in establishing the equilibrium level of $k_{\rm SGS}$ shown in Figure 3(b). A parallelism may be established between Eq. (4.1), and the corresponding transport equations for the SGS variances of the thermal energy and product mass fraction, $c_v^2\widetilde{T''^2} = c_v^2\widetilde{T^2} - c_v^2\widetilde{T}^2$ and $\widetilde{Y''^2} = \widetilde{Y^2} - \widetilde{Y}^2$, respectively, which are given by

$$\frac{\partial}{\partial t}\left(\frac{\overline{\rho}\widetilde{Y''^2}}{2}\right) + \frac{\partial}{\partial x_i}\left(\frac{\overline{\rho}\widetilde{u}_i\widetilde{Y''^2}}{2}\right) = \frac{\partial}{\partial x_i}\left(\widetilde{Y}\overline{J_i} - \overline{YJ_i} + \widetilde{Y}\mathcal{J}_i + \frac{\overline{\rho}\widetilde{u}_i\widetilde{Y^2} - \overline{\rho}\widetilde{u_i Y^2}}{2}\right) + \overline{J_i\frac{\partial Y}{\partial x_i}} - \overline{J}_i\frac{\partial\widetilde{Y}}{\partial x_i} + \overline{\rho Y\dot{\omega}} - \overline{\rho}\widetilde{Y}\widetilde{\dot{\omega}} + \epsilon_{{\rm SGS},Y}, \tag{4.2}$$

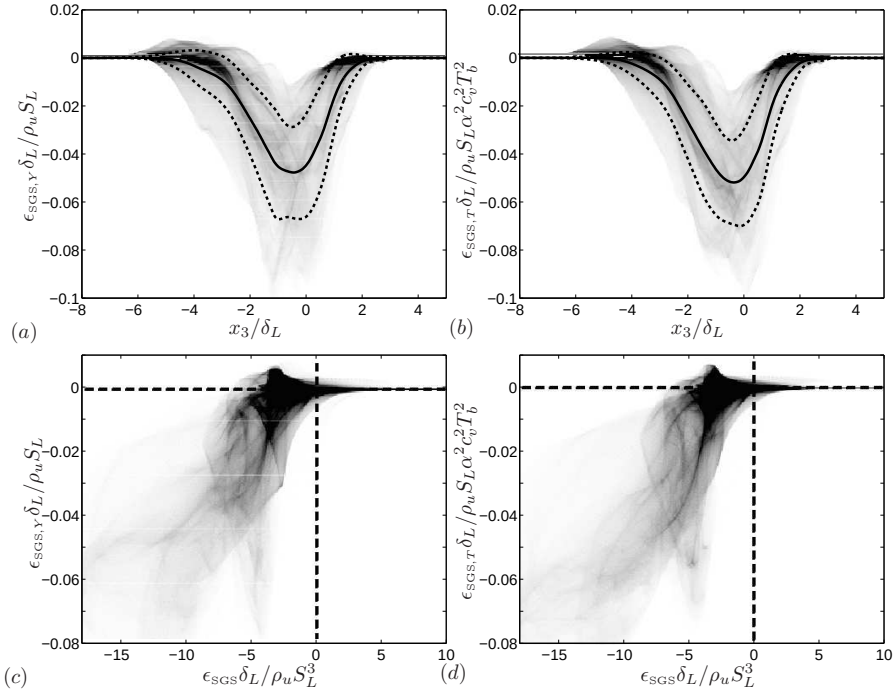

FIGURE 5. Contours of the PDF of (a) $\epsilon_{\mathrm{SGS},Y}$ and (b) $\epsilon_{\mathrm{SGS},T}$ conditioned on the streamwise coordinate x_3, including planar averages (solid lines) and standard deviations (dashed lines). Also shown in the future are the joint PDF contours of ϵ_{SGS} against (a) $\epsilon_{\mathrm{SGS},Y}$ and (b) $\epsilon_{\mathrm{SGS},T}$.

$$\frac{\partial}{\partial t}\left(\frac{\overline{\rho}c_v\widetilde{T''^2}}{2}\right)+\frac{\partial}{\partial x_i}\left(\frac{\overline{\rho}c_v\widetilde{u}_i\widetilde{T''^2}}{2}\right)=\frac{\partial}{\partial x_i}\left(\widetilde{T}\overline{q_i}-\overline{Tq_i}+\widetilde{T}\mathcal{Q}_i+\frac{\overline{\rho}c_v\widetilde{u}_i\widetilde{T^2}-\overline{\rho}\widetilde{u_iT^2}}{2}\right)$$
$$-\overline{P\Delta_v T}+\overline{P\Delta_v}\widetilde{T}+\overline{\tau_{ij}S_{ij}T}-\overline{\tau_{ij}S_{ij}}\widetilde{T}+\overline{\rho qT\dot{\omega}}-\overline{\rho}q\widetilde{T}\widetilde{\dot{\omega}}+\epsilon_{\mathrm{SGS},T}. \quad (4.3)$$

In Eqs. (4.2)-(4.3), $J_i=-\rho D\partial Y/\partial x_i$ and $q_i=-\lambda\partial T/\partial x_i$ are molecular fluxes of mass and heat, respectively, while $\mathcal{J}_i=\overline{\rho}(\widetilde{u_iY}-\widetilde{u}_i\widetilde{Y})$ and $\mathcal{Q}_i=\overline{\rho}c_v(\widetilde{u_iT}-\widetilde{u}_i\widetilde{T})$ represent their turbulent counterparts.

Although the detailed analysis of Eqs. (4.2)-(4.3) is beyond the scope of this report, it is of some interest to note the presence of the unclosed pseudo-dissipation terms

$$\epsilon_{\mathrm{SGS},Y}=-\mathcal{J}_i\frac{\partial\widetilde{Y}}{\partial x_i},\quad \epsilon_{\mathrm{SGS},T}=-\mathcal{Q}_i\frac{\partial\widetilde{T}}{\partial x_i}. \quad (4.4)$$

In a similar way as backscatter participates in modulating the updraft of SGS kinetic energy, the pseudo-dissipations $\epsilon_{\mathrm{SGS},Y}$ and $\epsilon_{\mathrm{SGS},T}$ also become statistically negative in the flame region in an attempt to evacuate the corresponding energy from SGS variances and transfer it to the resolved field, as illustrated in Figure 5(a,b). For the most part of the flame brush, simultaneous occurrence of backscatter ($\epsilon_{\mathrm{SGS}}<0$), $\epsilon_{\mathrm{SGS},Y}<0$ and $\epsilon_{\mathrm{SGS},T}<0$ is observed in more than 40% of the points, as shown in Figure 5(c,d). This effect, in turn, can be related to counter-gradient transport of scalars, as described below.

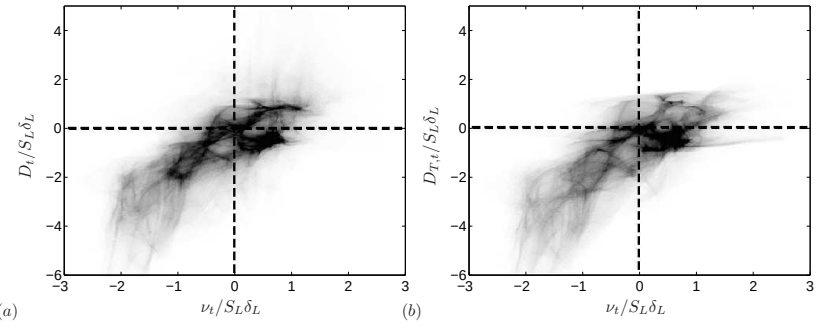

FIGURE 6. Contours of the joint PDF of the eddy viscosity ν_t against (a) species eddy diffusivity D_t and (b) thermal eddy diffusivity $D_{T,t}$ in the flame brush.

5. Counter-gradient subgrid-scale transport in the turbulent flame brush

Conditions corresponding to the occurrence of counter-gradient diffusion of scalars typically involve large thermal expansion ratios and low turbulent intensities, as in the present investigation. In this limit, the large-scale velocity fluctuations in the fresh turbulent gases, u_ℓ, become comparable to or larger than the characteristic velocity augmentation normal to the flame due to heat release, $u_\ell \sim S_L\alpha/(1-\alpha)$, thereby yielding Bray numbers of order unity or larger (Bray 1995). As a result, the prevailing acceleration of the flow in the forward streamwise direction, which was described in Section 3 in the context of non-Boussinesq transport, overcomes the tendency of turbulent eddies to stir the scalars in the burnt region and mix them back with fresh gases upstream from the flame.

In the LES context, the corresponding gradient expressions for species and thermal-energy turbulent transport become

$$\mathcal{J}_i = -\overline{\rho} D_t \frac{\partial \widetilde{Y}}{\partial x_i}, \quad \mathcal{Q}_i = -\overline{\rho} c_v D_{T,t} \frac{\partial \widetilde{T}}{\partial x_i},$$

where D_t and $D_{T,t}$ are, respectively, the eddy coefficients of species and thermal diffusion, whose values are mostly determined by the streamwise dynamics. Similar expressions to Eq. (3.6) can be derived to evaluate D_t and $D_{T,t}$ from the DNS by multiplying by the gradients of mass fraction and temperature, namely

$$D_t = \frac{\epsilon_{\mathrm{SGS},Y}}{\overline{\rho}\left(\partial\widetilde{Y}/\partial x_i\right)^2}, \quad D_{T,t} = \frac{\epsilon_{\mathrm{SGS},T}}{\overline{\rho} c_v \left(\partial\widetilde{T}/\partial x_i\right)^2}, \tag{5.1}$$

which minimize the fitting error in the least-squares sense and imply connections with the pseudo-dissipations of SGS variances $\epsilon_{\mathrm{SGS},Y}$ and $\epsilon_{\mathrm{SGS},T}$ defined in Eq. (4.4).

Of particular interest for LES-modeling purposes is to notice the simultaneous occurrence of counter-gradient diffusion of scalars and the transport of momentum against the Boussinesq approximation. This is observed in Figure 6, where approximately 40% of the points lie in the lower left quadrants as an indirect consequence of the correlations between backscatter and the pseudo-dissipations (4.4). These results suggest that palliation of counter-gradient transport, through particular LES closures or combustion models, may require additional consideration of a correspondingly appropriate closure for SGS momentum transport that correctly captures the non-Boussinesq dynamics.

6. Concluding remarks

In this study, DNS were employed to compute a turbulent deflagration in a parameter regime of interaction between the undisturbed flame and the forced turbulence, which was prone to develop counter-gradient diffusion. Differentially filtering and planar-averaging the DNS results revealed intense backscatter in the flame that prevailed over forward-scatter. Similarly, the flame brush was characterized in its entirety by dominant counter-gradient diffusion of scalars that occurred simultaneously with non-Boussinesq transport of momentum. This anomalous transport was connected to the strongly anisotropic updraft of SGS kinetic energy that results from a balance between the energy injected by thermal expansion, enabled by the chemical heat deployed in the flame, and its backscatter into the resolved field. Future directions of this work may involve the revision of algebraic RANS closures for scalars (Veynante *et al.* 1997; Robin *et al.* 2012) to account for accelerating thermal expansion effects in LES of turbulent deflagrations, along with consideration of appropriate momentum closures consistent with the persistent dynamics of kinetic-energy backscatter observed in the simulations.

Acknowledgments

The authors are grateful to Dr. Chiping Li, C. Towery and Dr. Hemanth Kolla for helpful discussions during the Summer Program.

REFERENCES

Aldredge, R. C. & Williams, F. A. 1991 Influence of wrinkled premixed-flame dynamics on large-scale, low-intensity turbulent flow. *J. Fluid Mech.* **228**, 487–511.

Aluie, H., Li, S. & Li, H. 2012 Conservative cascade of kinetic energy in compressible turbulence. *Astrophys. J. Lett.* **751**, 1–6.

Bray, K. N. C. 1995 Turbulent transport in flames. *Proc. R. Soc. Lond. A* **451**, 231–256.

Domaradzki, J. A. & Rogallo, R. S. 1990 Local energy transfer and nonlocal interactions in homogeneous, isotropic turbulence. *Phys. Fluids.* **2**, 413–426.

Ghosal, S., Lund, T. S., Moin, P. & Akselvoll, K. 1995 A dynamic localization model for large-eddy simulation of turbulent flows. *J. Fluid Mech.* **286**, 229–255.

Hamlington, P. C., Poludnenko, A. Y. & Oran, E. 2011 Interactions between turbulence and flames in premixed reacting flows. *Phys. Fluids* **23**, 125111.

Knauss, R. & Pantano, C. 2009 On the effect of heat release in turbulence spectra of non-premixed reacting shear layers. *J. Fluid Mech.* **626**, 67–109.

O'Brien, J., Urzay, J., Ihme, M., Moin, P. & Saghafian, A. 2014 Subrid-scale backscatter in reacting and inert supersonic hydrogen-air turbulent mixing layers. *J. Fluid Mech.* **743**, 554–584.

Peters, N. 2000 *Turbulent Combustion*. Cambridge University Press.

Piomelli, U., Cabot, W. H., Moin, P. & Lee, S. 1991 Subgridscale backscatter in turbulent and transitional flows. *Phys. Fluids A* **3**, 1766–1771.

Robin, V., Mura, A. & Champion, M. 2012 Algebraic models for turbulent transports in premixed flames. *Combust. Sci. Technol.* **184**, 1718–1742.

Sagaut, P. & Cambon, C. 2008 *Homogeneous Turbulence Dynamics*. Cambridge University Press.

Veynante, D., Trouvé, A., Bray, K. N. C. & Mantel, T. 1997 Gradient and counter-gradient scalar transport in turbulent premixed flames. *J. Fluid Mech.* **332**, 263–293.